Cortical synaptic vulnerabilities revealed in a α-synuclein aggregation model of Parkinson's disease

Saroj Sah [1,7], Andrew D. Sauerbeck [2,7], Jyoti Gupta [3,7], Dayana Pérez-Acuña [1,7], Jacob E. Reiber [5,7], Dreson L. Russell [5,7], Thomas M. Goralski [6,7], Michael X. Henderson [6,7], Laura A. Volpicelli-Daley [5,7], Michael J. Higley [3,4,7], Terrance T. Kummer [2,7] and Thomas Biederer [1,3,7] *

[1] Department of Neurology, Yale School of Medicine, New Haven, CT 06510, USA
[2] Department of Neurology, Washington University School of Medicine, St. Louis, MO 63110, USA
[3] Department of Neuroscience, Yale School of Medicine, New Haven, CT 06510, USA
[4] Department of Biomedical Engineering, Yale School of Medicine, New Haven, CT 06510, USA
[5] University of Alabama at Birmingham, Birmingham, AL 35294, USA
[6] Department of Neurodegenerative Science, Van Andel Institute, Grand Rapids, MI 49503
[7] Aligning Science Across Parkinson's (ASAP) Collaborative Research Network, Chevy Chase, MD

* Correspondence should be addressed to Thomas Biederer, thomas.biederer@yale.edu

Running Title: Cortical synaptopathy in Parkinson's disease

Keywords: Parkinson's disease; α-synuclein; cortex; synapse; excitation/inhibition imbalance

Abstract

Cognitive impairment is a frequent non-motor symptom in Parkinson's disease, and cortical Lewy pathology is strongly associated with cognitive decline. Synaptic pathology has been observed in the PD cortex, but the extent of synaptic vulnerabilities and their temporal and spatial relationship to pathology remains unclear. We employed high-resolution imaging to analyze synaptic abnormalities in layer 5 of the secondary motor cortex. We used striatal injections of α-synuclein pre-formed fibrils as a model to cause the progressive pathological aggregation of endogenous α-synuclein. We find that cortical α-synuclein pathology results in the progressive loss of excitatory synapses, followed by a reduction in inhibitory postsynaptic sites. Synapse loss is most pronounced in areas with high pathology. Additionally, we observed ultrastructural changes in the remaining excitatory synaptic loci, including smaller synaptic vesicles. Consistent with these results, gene ontology analysis of synaptic genes exhibiting altered expression in pathological neurons supported pre- and post-synaptic changes, including in synapse organizing pathways. Our results demonstrate that α-synuclein aggregation in the cortex is linked to molecular and structural alterations that disrupt synaptic connectivity and provide insights into the progressive PD-relevant vulnerability of cortical synapses.

Introduction

Parkinson's disease (PD) features both motor and non-motor impairments (Poewe et al., 2017). Up to 80% of PD patients develop cognitive changes, with a 6-fold increased risk of progression to dementia (Aarsland et al., 2021; Buter et al., 2008; Hely et al., 2008). Cortical Lewy pathology correlates with cognitive decline in PD (Braak et al., 2006; Irwin et al., 2017; Irwin et al., 2012; Ryman et al., 2021). Deficits in cognition have already been observed at the early stages of the disease, with a spectrum of abnormalities such as impaired working memory, visuospatial functions, and language (Caviness et al., 2011). The underlying molecular and cellular aberrations in the neocortex are mainly unknown.

A significant hallmark of the disease is the abnormal aggregation of the protein α-synuclein that is endogenously enriched at presynaptic sites into Lewy bodies and Lewy neurites. Lewy bodies and neurites are present across multiple brain regions beyond the substantia nigra, including limbic and cortical regions, and their abundance strongly correlates with cognitive decline and psychiatric symptoms in PD (Irwin et al., 2012; Schapira et al., 2017). Cortical dysfunction and morphological alterations have been described in PD (Bruck et al., 2005; Caviness et al., 2011; Li et al., 2022), supporting the relevance of neocortical circuit dysfunction in cognition. Propagation of misfolded α-synuclein is a key pathological event in PD, where abnormally aggregated α-synuclein species serve as templates that seed the conversion of monomeric α-synuclein into inclusions as the disease progresses (Braak et al., 2003; Recasens et al., 2014). This phenomenon has been modeled and reproduced *in vivo* using pre-formed fibrils (PFFs) comprised of *in vitro* assembled β-sheet-rich α-synuclein. Once injected into the brain, PFFs recapitulate aspects of PD Lewy body pathology (Henderson et al., 2019), causing dysregulation in multiple cellular and molecular pathways (Goralski et al., 2024) and leading to neuroinflammation (Earls et al., 2019; Iba et al., 2022), metabolic impairment (Creed et al., 2022; Lu et al., 2022) and circuit dysfunction (Blumenstock et al., 2021). This can be analyzed to measure the progression of pathology between anatomically connected neuronal populations, including in cortical neurons projecting to the striatum (Henderson et al., 2019; Luk et al., 2012).

α-Synuclein is enriched in the presynaptic terminal, and the three members of this protein family shape synaptic architecture (Vargas et al., 2017). This suggested that synapses could be

vulnerable sites for α-synuclein pathology and synaptopathy could be among the first pathological processes in multiple neurodegenerative diseases, including PD (Schirinzi et al., 2016). Indeed, brain imaging studies have shown a loss of synaptic markers in PD patients (Matuskey et al., 2020), and dendritic spine loss has been reported in other synucleinopathies (Kramer and Schulz-Schaeffer, 2007). Post-mortem studies of PD, PDD, and Dementia with Lewy Bodies show reduced synaptic marker density in the cortex that is correlated with the extent of Lewy pathology (Frigerio et al., 2024; Thomsen et al., 2021). It has been proposed that a reduction in synaptic vesicle proteins in the prefrontal cortex could be a potential cause of dementia in patients with PD (Holmes et al., 2024). Indeed, in experimental models, it has been reported that α-synuclein aggregation impairs excitatory neuron transmission and connectivity (Blumenstock et al., 2017; Chen et al., 1996; Froula et al., 2018; Volpicelli-Daley et al., 2011).

Here, we aim to define synaptic aberrations in PD to understand alterations in cortical connectivity that can underlie cognitive impairments. As an approach, we use intrastriatal PFF injection to address the extent to which cortical synapses are a cellular locus for dysfunction in PD. We analyze layer 5 of the secondary motor cortex, as it includes intratelencephalic (IT) neurons that project to the striatum as a subpopulation of neurons that preferentially develops α-synuclein aggregates (Goralski et al., 2024), including spine and synapse loss and exhibit dendrite malformation (Blumenstock et al., 2017; Pérez-Acuña et al., 2023). Tracking the gradual increase in α-synuclein pathology, we measured a reduction of synapses proximal to areas with high pathology. SEQUIN high-resolution imaging determined that cortical pathology impacts excitatory synapses after a lag period, and they were then progressively lost. Structural changes were observed in the remaining excitatory synapses, including physical separation of synapses and enlargement of pathology-bearing presynaptic sites. Using EM, we observed reduced synaptic vesicle volumes and shortened postsynaptic sites. After excitatory synapse pathology appeared, inhibitory postsynaptic sites were lost. These pathologies matched our synaptic gene ontology analysis of gene expression alterations in pathology-bearing neurons conserved between PD brain and mice injected with α-synuclein PFFs (Goralski et al., 2024). We additionally determined that cortical α-synuclein pathology in this PFF model results in substantial aberrations of excitatory transmission. Together, this work delineates synapse-type

75 vulnerabilities in the cortex that result from α-synuclein pathology on molecular, cellular, and
76 functional levels.

Results

Progressive excitatory synapse loss in the prefrontal cortex is associated with α–synuclein pathology. Both human and PFF mouse models have revealed that excitatory neurons are most likely to bear a higher abundance of α– synuclein inclusions in layer 5 of the prefrontal cortex. Furthermore, it has been validated in the PFF mouse model that α-synuclein-inclusion-positive excitatory neurons have downregulated differentially expressed genes (DGEs) for VGlut1 and Homer (Goralski et al., 2024). Thus, we analyzed the distribution of excitatory synapses by measuring the immunoreactivity of VGluT1 and Homer using SEQUIN in the layer 5 prefrontal cortex of mice injected into the dorsolateral striatum with PFFs. Monomer-injected mice served as controls.

Mice exhibited α–synuclein inclusions in the prefrontal cortex 1 month post-injection (MPI) of PFFs in the striatum as reported, which plateaued at 3 months, while no inclusions appeared after monomer injection, which served as control (Luk et al., 2012) (Figure 1A and Supplementary Fig 1). SEQUIN identifies synaptic loci by recognizing separations of pre- and post-synaptic markers consistent with ultrastructural parameters and utilizes an enhanced image resolution methodology (Sauerbeck et al., 2020). Staining for the excitatory pre- and post-synaptic markers VGluT1 and Homer followed by SEQUIN analysis showed no apparent change in the density of pre-and post-synaptic pairs containing both VGluT1/Homer in striatally PFF-injected mice compared with monomer-injected mice at 1 MPI (Fig.1B). Interestingly, we identified that the abundance of paired excitatory VGluT1/Homer synaptic loci was lower in the prefrontal cortex 3 months after striatal PFF injection compared to monomer-injected mice (monomer: 0.086 ± 0.003 / μm^3 vs PFF: 0.076 ± 0.003 / μm^3, $p = 0.042$) (Fig.1C). The decrease in excitatory synaptic loci persisted at 6 MPI, with a reduction in density (monomer: 0.066 ± 0.002 / μm^3 vs PFF: 0.060 ± 0.002 / μm^3, $p=0.018$) (Fig.1D)

Fewer total excitatory specializations at 3 months post-PFF injection. Analysis of the SEQUIN imaging data by Imaris showed no change in the density of total VGluT1 and Homer puncta at 1 MPI, irrespective of whether they were within the synaptic loci (Fig.2A). The loss of synapses at

106 3 MPI was coupled with a decreased number of total VGluT1 puncta and Homer puncta (Fig.2B).
107 No changes in the VGluT1 and Homer puncta were observed at 6 MPI (Fig.2C). This could indicate
108 that a compensatory improvement in the alignment of synaptic markers at later stages of
109 α–synuclein pathology.
110
111 **A reduction in cortical inhibitory postsynaptic sites follows excitatory synapse loss.** The extent
112 of the vulnerability of different synapse subtypes to α–synuclein pathology is unknown. We
113 performed SEQUIN analysis to study whether inhibitory synapses are affected by synuclein
114 inclusion in the prefrontal cortex of PFF-injected mice compared to control mice injected with
115 monomers. Staining for inhibitory presynaptic VGAT and inhibitory postsynaptic Gephyrin
116 revealed no significant changes in the density of synaptically paired or total VGAT or Gephyrin at
117 3 MPI (Fig.3A). However, the number of postsynaptic gephyrin puncta was reduced at 6 MPI
118 (Fig.3B). This impact on inhibitory synaptic markers was therefore subsequent to the loss of
119 excitatory synapses and may reflect a homeostatic balancing mechanisms to partially restore
120 excitation/inhibition balance rather than direct synaptic pathology caused by a-synuclein
121 aggregates.
122
123 **Localization of phospho-α-synuclein aggregates relative to synaptic loci after PFF injection.** We
124 next addressed to what extent synapses are marked by a-synuclein pathology. One month after
125 either monomer or PFF injection into the striatum, the synaptic proteins PSD-95 and synapsin, as
126 well as phosphorylated α-synuclein, were imaged at enhanced resolution in 3-dimensional
127 volumes of the fronal cortex (Fig.4A). Co-staining with an antibody against pS129 phospho-α-
128 synuclein that marks the aggregated pathological form of this protein was detected in close
129 association with apparent synaptic loci (Fig.4B). To quantify synaptic localization of phospho-α-
130 synuclein, SEQUIN was employed to identify synaptic loci and measure the amount of phospho-
131 α-synuclein associated with each locus (within a 200 nm field centered on the centroid of each
132 SEQUIN-identified synaptic locus) (Fig.4C). Compared to monomer treatment, an elevation in
133 synapse associated phospho-α-synuclein was observed following PFF treatment (Fig.4D, PFF-
134 effect, p=0.1 Mann-Whitney U test.). Regardless of the general level of pathology, all areas

assessed exhibited an increase in synapse-associated phospho-α-synuclein relative to parenchymal levels, indicative of specific synaptic enrichment (Fig.4D). The ratio between synapse-associated and parenchymal phospho-α-synuclein tended to be higher as the overall level of pathology increased (Fig.4E, p=0.0786 Kruskal-Wallis on group average).

Mesoscale analysis of the impact of phospho-a-synuclein pathology on synaptic density after PFF injection. We aimed to complement the high-resolution analysis of synaptic puncta with a mesoscale quantification of how α-synuclein pathology impacts synaptic distribution. Cortical mesoscans of synaptic proteins and phospho-α-synuclein were collected from animals 1 MPI of either monomer or PFF (Fig.4F-H). For both the monomer and PFF treatment groups, average heatmaps of synaptic density and synapse-associated phospho-α-synuclein were generated (Fig.4I-L). Areas of elevated synapse-specific phospho-α-synuclein in these heatmaps were associated with an overall reduction in synaptic density, a trend that was also apparent on quantitative analysis (Fig.4M, note the modest group sizes and model variability preclude drawing firm conclusions based on statistical analysis: p=0.4 Mann-Whitney U test, Fig.4N p= 0.1 Mann-Whitney U test). To explore these effects further, within animal analysis of synaptic density and synapse-associated phospho-α-synuclein levels were performed (Fig.4O-Q). In two of the three PFF-treated subjects, a significant, negative correlation was detected between phospho-α-synuclein level and synaptic density (Fig.4O,P), while a third animal exhibited a positive correlation (Fig.4Q). These data provide further evidence of synapse loss in response to synuclein-related pathology.

Synapse-associated phospho-α-synuclein and synaptic density are associated with proximity to Lewy neurites. We next addressed the spatial relationship of cortical phospho-a-synuclein aggregates formed after striatal PFF injection and synaptic aberrations. At 1 MPI of PFF, synapses were identified using SEQUIN (Fig.5A). In these same areas, phospho-a-synuclein was imaged and used to identify Lewy neurites (Fig.5A-B). The distance to the closest Lewy neurite edge was measured for each synaptic centroid (Fig.5C). A significant association was observed between the proximity of a synaptic locus to a Lewy neurite and the enrichment of phospho-a-synuclein at the

same synaptic locus (Fig.5D). To gain insight into the implications of this effect, the density of synaptic loci with 800 μm of the perimeter of Lewy neurites with varying degrees of pathology (as assessed by total intra-neuritic phospho-α-synuclein levels) was quantified. This analysis revealed a significant, negative association between synaptic density and Lewy neurite pathology (Fig.5E). These results suggest that Lewy neurites locally impact synapses, leading to their loss.

Analysis of dysregulated synaptic pathways in πηοσπηο–α–σψνυχλειν bearing neurons using SYNGO database. We further analyzed gene enrichment of synaptic pathways in pS129 phospho-α-synuclein bearing neurons from previous transcriptomic results (Goralski et al., 2024) by using SynGO, a database for synaptic ontology (Koopmans et al., 2019). After comparing the LAMDA (Lewy-associated molecular dysfunction from aggregates) signature from 3 months after injection mice, against the 1602 annotated genes in the SYNGO database, we found that 1306 genes were identified in this transcriptomic analysis. Among these, 469 were differentially expressed genes, with 418 of them downregulated and 51 upregulated in phospho-α-synuclein positive neurons (Fig.6A and Supplemental Fig.2). Enrichment analysis from genes downregulated showed that by cellular component, genes from postsynaptic density and synaptic vesicles were overrepresented (Fig.6B). Biological processes from these DEGs corresponded to the synaptic organization, presynaptic vesicle cycle, and processes in the post-synapse (Fig.6C). Markers used for our synaptic density analyses, vGlut1 and Homer1, were downregulated. In the case of the markers vGAT and Gephrin, we did not find a decrease in their expression, which was expected for vGAT as pathological neurons are excitatory.

For upregulated genes, cellular component enrichment, similar to downregulated genes, included terms annotated in synaptic specialization and postsynaptic membranes (Fig.4D). Biological processes also included synaptic organization, processes in the post-synapse, and synaptic signaling. We noted enrichment of GPC6 (glypican 6) and TNM2 (teneurin 2), regulators of neurotransmitter receptor localization for postsynaptic specialization and synapse maintenance, suggesting that neurons with pathology might activate response mechanisms to promote and sustain synaptic activity.

193 **A separation of excitatory pre- and post-synaptic specializations is accompanied by**
194 **ultrastructural changes.** Based on our SYNGO analysis of DEGs, we hypothesized that synuclein
195 inclusions may also contribute to nanostructure aberrations in the synapses. Using SEQUIN, we
196 measured the average pre- and post-synaptic separation for VGluT1 and Homer at 1 MPI and at
197 3 MPI, the timepoint when we observed a decrease in excitatory synapses. The Gaussian
198 distribution of the pre- and post-synaptic separation for synaptic loci showed no change at 1 MPI
199 but revealed an increased mean separation for VGluT1/Homer pairs in the prefrontal cortex at 3
200 MPI of PFF fibrils compared to monomers in mice (Fig.7A,B).

201 Our findings were further supported by ultrastructural analysis using transmission electron
202 microscopy, which demonstrated a reduction in the size of synaptic vesicles in PFF-injected mice
203 compared to control mice (Fig.7C). These nanostructure changes could potentially contribute to
204 the increased separation between pre- and post-synaptic proteins in excitatory synapses positive
205 to VGluT1/Homer.

Discussion

The abnormal accumulation of α–synuclein into inclusions, known as Lewy bodies, is a major hallmark of PD and responsible for dopaminergic neuronal loss. These inclusions and neurites are widespread across brain regions beyond the substantia nigra, including limbic and cortical regions. Their presence strongly correlates with cognitive decline in PD (Irwin et al., 2012; Schapira et al., 2017). PD is associated with cortical dysfunction and morphological alterations (Bruck et al., 2005; Caviness et al., 2011; Li et al., 2022), highlighting the relevance of neocortical circuit dysfunction in cognitive impairment. A reduction in the presynaptic marker synaptophysin in the pyramidal layer of the neocortex is considered a significant factor in the development of dementia in Parkinson's disease (Zhan et al., 1993). A recent study confirmed the loss of synaptic vesicle glycoprotein 2A in the cortex in both Parkinson's disease dementia and dementia with Lewy bodies, supporting that pathological changes and subsequent synapse loss extend beyond the substantia nigra to affect the cortex, contributing to cognitive impairment (Andersen et al., 2021). However, the specificity of synapse loss and the nanostructural aberrations contributing to mechanobiological changes contributing with cognitive deficits remain poorly investigated. The prefrontal cortex is considered the essential brain region that is affected by PD cognitive impairment (Cai et al., 2021). To address these pathophysiological aspects of synapse-specific aberrations in the prefrontal cortex, we injected pre-formed fibrils (PFFs) into mice to replicate cortical alpha-synuclein inclusion pathology resembling Lewy bodies and Lewy neurites found in humans, and briefly investigated resulting synaptic aberrations in this region.

We observed α–synuclein inclusions in the secondary motor prefrontal cortex after 1 month of PFF injection in the striatum, although there was no change in synapse loci nor in the number of pre-/postsynaptic proteins positive for VGluT1/Homer. By the 3-month mark, we noted a reduction in excitatory synaptic loci accompanied by decreased levels of both VGluT1 and Homer. This suggests that the loss of excitatory synapses at this time point may be attributed to prolonged exposure to p-Syn inclusions and progressive synuclein pathology. Our data further revealed persistent synapse loss 6 months post-PFF injection, although changes in VGluT1 and Homer puncta were compensated. Analysis using the SYNGO database indicated upregulation of specific genes promoting synaptic protein formation in response to PFF injection, supporting

235 compensatory upregulation of synaptogenic pathways and the generation of orphan synaptic
236 sites. These findings underscore the relevance of overall excitatory synapse loss during the later
237 stages of disease pathology development. The enrichment of pathological phospho-α-synuclein
238 at synapses may contribute to their widespread loss following PFF injection.

239 Our in vivo findings align with previously reported in vitro data demonstrating that PFF
240 treatment compromises excitatory synaptic activity in a time- and dose-dependent manner. The
241 severity of these deficits correlates with the formation of αSyn pathology in cultured excitatory
242 hippocampal neurons (Wu et al., 2019). We observed the least pronounced effect on
243 postsynaptic inhibitory proteins, with no apparent overall loss of inhibitory synapses. This
244 minimal or absent impact on inhibitory synapses may be due to fewer synuclein inclusions in
245 inhibitory neurons compared to excitatory neurons in layer 5 of the secondary motor cortex
246 (Goralski et al., 2024). where we also conducted synaptic aberration analysis. Our results
247 highlight differential vulnerabilities across synapse types, reflecting varied expression of alpha-
248 synuclein pathology within specific neuron populations in layer 5 of the secondary motor cortex.

249 We identified an increased separation between VGluT1 and Homer in the cortex after 3 and
250 6 months PFF post-injection. This stretched separation indicates a potential shift in the
251 localization of pre- and postsynaptic proteins or a decrease in network connectivity at synaptic
252 loci, which can potentially lead to defects in neurotransmission and synapse stability (Frye et al.,
253 2021). Furthermore, reductions in synaptic vesicle and postsynaptic density sizes at synaptic loci,
254 as shown by ultrastructural analysis, could also be a cause of these aberrant phenotypes. These
255 alterations to synaptic architecture may contribute to behavioral deficits (Gcwensa et al., 2024),
256 including cognitive impairment. The downregulation of pathways involved in synapse
257 organization, as indicated by analysis of dysregulated synaptic pathways in phospho-α-synuclein
258 bearing neurons using SYNGO database, in PFF-injected mice could be the mechanistic approach
259 involved in the nanostructural aberrations we observed within excitatory synapses.

Materials and Methods

Antibodies. Primary antibodies and application notes for immunohistochemistry (IHC) are provided in Table 1. Secondary antibodies, including isotype-specific ones to detect monoclonal primary antibodies, were conjugated to Alexa dyes 405, 488, 568, and 647 (Thermo Fisher) and incubated overnight at 4 °C.

Target	Vendor	Cat. No.	RRID	Host	Clonality	Application IHC
VGluT1	Synaptic Systems	135 304	AB_887878	Guinea Pig	Polyclonal	1:200 (48 h, RT)
Homer	Synaptic Systems	160 003	AB_887730	Rabbit	Polyclonal	1:250 (48 h, RT)
VGAT	Synaptic Systems	131 003	AB_887869	Rabbit	Polyclonal	1:250 (36 h at 4 °C)
Gephyrin	Synaptic Systems	147 111	AB_887719	Mouse	Monoclonal IgG1	1:250 (36 h at 4 °C)

Table 1. Primary and secondary antibody applications.

Animals. Studies were performed using 3-month-old wild-type C57BL/6J mice obtained from Jackson Laboratories (Bar Harbor, ME, USA). Both female and male mice were included in the study unless otherwise stated. All animal procedures undertaken in this study to generate SEQUIN or immunochemistry data were approved by the Yale University Institutional Animal Care & Use Committee and complied with the National Institutes of Health guidelines for the Care and Use of Laboratory Animals.

Preparation of recombinant α-synuclein monomer and preformed fibrils. Monomeric mouse α-synuclein was expressed in E. coli and purified, followed by endotoxin removal using Pierce LAL high-capacity endotoxin removal resin, as previously described (Volpicelli-Daley et al., 2014). The monomer was stored at −80°C. Preformed fibrils (PFFs) at a concentration of 5 mg/mL were produced from monomeric α-synuclein by agitation in 150 mM KCl/50 mM Tris-HCl at 37°C for seven days (Bousset et al., 2013; Stoyka et al., 2020). PFFs in a volume of 22-25 µL were placed in a 1.5 mL sonicator tube (Active Motif, NC0869649) and sonicated for 15 min at an amplitude of 30, with a pulse on and off for 3 sec and 2 sec, respectively. The resulting PFF fragments, ranging from 20 to 70 nm, were verified by dynamic light scattering and stored at -80°C until needed. On the day of injection, the sonicated PFFs were re-sonicated for 15 min at an amplitude of 40, with a pulse on and off for 3 s, respectively, at 10°C and used within 8 h. The PFFs were kept at room temperature during the injections. In contrast, the monomer was kept on ice during the injections to prevent aggregation.

Stereotaxic injections of recombinant proteins. Mice were deeply anesthetized using isoflurane vaporizer (Harvard Apparatus Mobile Anesthesia System, model 750239) and placed on a

292 stereotactic frame (Kopf, model 900 LS). Thereafter, mice were unilaterally injected with 2 µL (5
293 mg/mL) of either PFFs or monomer (as a control) into the right forebrain at coordinates +0.2 mm
294 relative to Bregma, +2.0 mm from midline, and -2.6 mm beneath the dura to target the dorsal
295 striatum. The injection was performed using a Nanoject III microinjector (Drummond Scientific)
296 at a rate of 20 nL/s over 100 cycles with a delay of 8 s between cycles. The needle remained
297 undisturbed for 10 min after the protein delivery inside the dorsal striatum and was gradually
298 withdrawn to prevent backflow or leakage into the cortex.
299
300 **Tissue processing for SEQUIN synapse quantification.** SEQUIN enables enhanced resolution of
301 synapses, allowing to measure pre- and post-synaptic pairs on a 3D mesoscale (Sauerbeck et al.,
302 2020). SEQUIN multiscale imaging was used to quantify synaptic loci in layer 5 of the prefrontal
303 cortex and characterize synaptic nanostructural properties at the individual and population
304 levels, as previously described (Reitz et al., 2021). In brief, mice injected with either monomer or
305 PFFs, 1, 3, or 6 months post-injection, were deeply anesthetized by intraperitoneal ketamine (100
306 mg/kg) and xylazine (10 mg/kg) cocktail injection and transcardially perfused using a 27G needle
307 at a rate of 6 ml/min with ice-cold 1x Phosphate Buffered Saline (PBS) for 4 min, followed by ice-
308 cold 4% formaldehyde (PFA) in PBS (pH 7.6) for 4 min. The brains were then extracted and post-
309 fixed for 24 h at 4°C in 4% PFA in PBS and stored in PBS at 4°C in scintillation vials protected from
310 light. Fixed brains were sectioned coronally into 40 µm-thick slices using a vibratome (Leica
311 VT1000 S). Brain slices were stored in 24-well plates in cryoprotectant buffer (PBS containing 30%
312 ethylene glycol, 30% sucrose, and 0.02% sodium azide) at −20°C.
313 Slices from the prefrontal cortex were washed 3 times for 5 min each in PBS, then blocked in
314 20% normal goat serum (Jackson ImmunoResearch) in PBS for 1 h at room temperature (RT).
315 Slices were then immunolabeled with primary antibodies and washed 3 times for 5 min each in
316 PBS, followed by Alexa Fluor-labeled secondary antibodies prepared in PBS containing 10% NGS
317 and 0.3% Triton X-100 in the dark (details on antibodies used and conditions are listed in Table
318 1). The slices were washed 3 times for 5 min each in PBS to remove the unbound secondary
319 antibodies, counterstained with DAPI in PBS for 10 min, rinsed 3 times for 5 min each in PBS,
320 transferred to charged microscopic glass slides, dried at RT, and rinsed in distilled water to
321 remove PBS residues. The slides were dried at RT and embedded in mounting media freshly
322 prepared by mixing Tris-MWL 4-88 (Electron Microscopy Sciences #17977-150, Hatfield, PA, USA)
323 with AF300 (Electron Microscopy Sciences #17977-25) in a 9:1 ratio with 1.5H coverglass. The
324 coverglass used for SEQUIN was stain-free, thoroughly cleaned with 100% ethanol, rinsed with
325 distilled water, and air-dried prior to coverslipping. The slides were cured at RT for 3 days.
326
327 **SEQUIN imaging of synapses and image analysis.** Images were obtained, processed, and
328 analyzed as previously described (Reitz et al., 2021) using a Zeiss LSM 900 Airyscan Microscope
329 (Carl Zeiss Microscopy) with 63x (numerical aperture 1.4) oil immersion objectives (6-8 images
330 per animal from 3 slices) and processed in 3D Airyscan. The channel alignment of the Airyscan-
331 processed images was inspected and corrected if required. Pre- and post-synaptic puncta were
332 detected as spots using Imaris 3D visualization software (Bitplane), and individual spots and
333 synaptic locations were quantified through a custom nearest neighbor analysis in MATLAB. The
334 code is available on GitHub: https://github.com/KummerLab/SEQUIN.

To quantify synapse density, the frequency distribution of nearest-neighbor pre- and post-synaptic protein pairs was generated for the top 20% intensity of pre- and post-synaptic puncta. The frequency distribution of nearest neighbor pairs, which forms a Gaussian distribution and excludes all random non-synaptic pairings, was used to calculate the synaptic locus density. The mean value calculated at the peak of the Gaussian distribution provided the average pre-post synaptic separation. The number of pre- and posts-synaptic puncta, including those randomly allocated and not associated with synaptic loci, irrespective of whether they were within synaptic loci, was quantified from the spot analysis using Imaris 3D visualization software.

GeoMx statistics and reproducibility.

Quality Control. In the mouse GeoMx experiment, 124 segments were collected in total from 11 mice, and 21 of these segments failed Quality Control (QC) analysis and were removed from the dataset. One segment was removed for sequence stitching < 80%, and aligned sequence reads < 75%. Five additional segments were removed for aligned sequence reads < 75% alone, and four segments were removed for sequence saturation < 50%. An additional 11 segments were removed for < 3% of genes being detected above the Limit of Quantification (LOQ). Of the 20175 gene targets contained in the GeoMx Mouse Whole Transcriptome Atlas, 9035 were included in the downstream analyses following QC analysis. 1 gene target was removed as a global outlier (Grubbs test, P<0.01), and 7 were removed as local outliers (Grubbs test, P<0.01). 211 genes were detected below the limit of quantification and were removed. Of the remaining gene targets, 9,031 gene targets were detected above the LOQ in at least 10% of segments, and therefore were selected for further analysis. An additional 4 gene targets were identified as interesting *a priori* and were retained in the study for additional analysis. Detailed QC parameters are described in our mouse analysis https://github.com/Goralsth/Spatial-transcriptomics-reveals-molecular-dysfunction-associated-with-cortical-Lewy-pathology (DOI: 10.5281/zenodo.10732492) Sample size was determined based on pilot data. No statistical method was used to determine sample size. Experiments did not involve multiple experimental conditions.

In the human GeoMx experiment, 238 segments were collected in total from 8 human PD/PDD/DLB cingulate cortex samples (n=6 male, n=2 female). The Human GeoMx data was assessed on the same parameters as the mouse tissue for Quality Control (QC). In total 63 segments failed QC and were removed from the dataset. 33 samples were removed for low sequence saturation, and 6 segments were removed for low area. An additional 24 segments were removed for < 5% of genes being detected above the Limit of Quantification (LOQ). Of the 18,815 gene targets present in the GeoMx Human Whole Transcriptome Atlas, 8,601 gene targets were included in the downstream analyses following QC. 9 gene targets were removed as local outliers (Grubbs test, P<0.01). 138 genes were detected below the limit of detection and were removed. Of the remaining gene targets, 8,595 gene targets were detected in at least 10% of segments. 6 gene targets were identified as interesting *a priori* and were retained in the study for additional analysis. Detailed QC parameters are described in our human analysis pipeline https://github.com/Goralsth/Spatial-transcriptomics-reveals-molecular-dysfunction-associated-with-cortical-Lewy-pathology (DOI: 10.5281/zenodo.10732492). Sample size was determined based on pilot data. No statistical method was used to determine sample size. Experiments did not involve multiple experimental conditions.

Normalization. To account for systematic variation between AOI's, we normalized each count by the 75th percentile (Q3) of expression for each AOI. To ensure normalization and Quality Control (QC) procedures were accurate, we compared each AOI's Q3 value to its limit of quantification. Normalization and QC procedures were determined to be adequate for robust downstream analysis.

Differential Expression. Differential expression of gene targets in the GeoMx experiments was determined via a mixed effects linear regression model. The regression model implemented was as follows: (1) *y*= gene ~ comparison of interest * variable to control + (1/individual). This model robustly tests for differential gene expression for comparisons of interest (ex. phospho-α-synuclein negative vs. phospho-α-synuclein positive brain region differences, etc.) while controlling for confounding variables and multiple sampling of the same samples.

Gene Set Enrichment Analysis. Gene Set Enrichment Analysis was implemented using the GSVA (Hanzelmann et al., 2013) (RRID:SCR_021058) package in R to determine disrupted pathways between neurons positive and negative for phospho-α-synuclein immunoreactivity. The minimum pathway size was set to 5 genes, and the maximum pathway size was set to 500 genes. We utilized Kegg Brite pathways to determine which transcriptional pathways are differentially expressed.

Cell-type deconvolution. We used nanoString's cell-type deconvolution algorithm, SpatialDecon (Danaher et al., 2022), to determine the cell-type proportions in our spatial transcriptomics data. We determined cell-type proportions in our data via comparison of our data to single-cell atlas data from the Allen Brain Institute via *SpatialDecon*'s log normal regression. To determine statistical significance of differences in cell type proportions between inclusion bearing (phospho-α-synuclein immunopositive) and non-inclusion bearing (phospho-α-synuclein immunonegative) segments, we utilized the following equation:

(2) *y*= cell-type proportion ~ inclusion status group + (1/individual)

GeoMx data availability. The raw sequencing files and associated metadata for both mouse and human experiments generated in this study have been deposited in the Sequence Read Archive (SRA): https://www.ncbi.nlm.nih.gov/sra/PRJNA1082339
The pre-quality control and supporting data for all experiments are available at the following Zenodo repository: https://zenodo.org/records/10729767 [95] (DOI: 10.5281/zenodo.10729767)

GeoMX code availability. Code used to generate the analyze gene expression and cell detection is available on GitHub: https://github.com/Goralsth/Spatial-transcriptomics-reveals-molecular-dysfunction-associated-with-cortical-Lewy-pathology [96] (DOI: 10.5281/zenodo.10732492).

SynGO enrichment analysis. The expert-curated SynGO gene ontology database (Koopmans et al., 2019) was used to characterize the GeoMX-derived synaptic transmission pathways enriched in differentially expressed genes from phospho-α-synuclein bearing neurons available from Goralski et al. studies. The list of DEGs was loaded against the 1602 annotated genes (SynGO release 1.2 '20231201'). For downregulated genes (enriched in phospho-α-synuclein immunonegative neurons), 418 genes were mapped (397 genes had a cellular component

420 annotation, and 299 had a biological process annotation). For upregulated genes, 51 were
421 mapped where 46 had a cellular component annotation, and 34 had a biological processes
422 annotation. Additionally, 40 and 18 cellular component terms, and 82 and 15 biological processes
423 were significantly enriched at 1% FDR for downregulated and upregulated genes respectively.
424

References

Aarsland, D., Batzu, L., Halliday, G.M., Geurtsen, G.J., Ballard, C., Ray Chaudhuri, K., and Weintraub, D. (2021). Parkinson disease-associated cognitive impairment. Nat Rev Dis Primers 7, 47.

Andersen, K.B., Hansen, A.K., Damholdt, M.F., Horsager, J., Skjaerbaek, C., Gottrup, H., Klit, H., Schacht, A.C., Danielsen, E.H., Brooks, D.J., and Borghammer, P. (2021). Reduced Synaptic Density in Patients with Lewy Body Dementia: An [(11) C]UCB-J PET Imaging Study. Mov Disord 36, 2057-2065.

Blumenstock, S., Rodrigues, E.F., Peters, F., Blazquez-Llorca, L., Schmidt, F., Giese, A., and Herms, J. (2017). Seeding and transgenic overexpression of alpha-synuclein triggers dendritic spine pathology in the neocortex. EMBO Mol Med 9, 716-731.

Blumenstock, S., Sun, F., Klaus, C., Marinkovic, P., Sgobio, C., Paeger, L., Liebscher, S., and Herms, J. (2021). Cortical circuit dysfunction in a mouse model of alpha-synucleinopathy in vivo. Brain Commun 3, fcab273.

Bousset, L., Pieri, L., Ruiz-Arlandis, G., Gath, J., Jensen, P.H., Habenstein, B., Madiona, K., Olieric, V., Bockmann, A., Meier, B.H., and Melki, R. (2013). Structural and functional characterization of two alpha-synuclein strains. Nat Commun 4, 2575.

Braak, H., Del Tredici, K., Rub, U., de Vos, R.A., Jansen Steur, E.N., and Braak, E. (2003). Staging of brain pathology related to sporadic Parkinson's disease. Neurobiol Aging 24, 197-211.

Braak, H., Rub, U., and Del Tredici, K. (2006). Cognitive decline correlates with neuropathological stage in Parkinson's disease. J Neurol Sci 248, 255-258.

Bruck, A., Aalto, S., Nurmi, E., Bergman, J., and Rinne, J.O. (2005). Cortical 6-[18F]fluoro-L-dopa uptake and frontal cognitive functions in early Parkinson's disease. Neurobiol Aging 26, 891-898.

Buter, T.C., van den Hout, A., Matthews, F.E., Larsen, J.P., Brayne, C., and Aarsland, D. (2008). Dementia and survival in Parkinson disease: a 12-year population study. Neurology 70, 1017-1022.

Cai, M., Dang, G., Su, X., Zhu, L., Shi, X., Che, S., Lan, X., Luo, X., and Guo, Y. (2021). Identifying Mild Cognitive Impairment in Parkinson's Disease With Electroencephalogram Functional Connectivity. Front Aging Neurosci 13, 701499.

Caviness, J.N., Lue, L.F., Beach, T.G., Hentz, J.G., Adler, C.H., Sue, L., Sadeghi, R., Driver-Dunckley, E., Evidente, V.G., Sabbagh, M.N., *et al.* (2011). Parkinson's disease, cortical dysfunction, and alpha-synuclein. Mov Disord 26, 1436-1442.

Chen, C., Kim, J.J., Thompson, R.F., and Tonegawa, S. (1996). Hippocampal lesions impair contextual fear conditioning in two strains of mice. Behav Neurosci 110, 1177-1180.

Creed, R.B., Memon, A.A., Komaragiri, S.P., Barodia, S.K., and Goldberg, M.S. (2022). Analysis of hemisphere-dependent effects of unilateral intrastriatal injection of alpha-synuclein pre-formed fibrils on mitochondrial protein levels, dynamics, and function. Acta Neuropathol Commun 10, 78.

464 Danaher, P., Kim, Y., Nelson, B., Griswold, M., Yang, Z., Piazza, E., and Beechem, J.M. (2022).
465 Advances in mixed cell deconvolution enable quantification of cell types in spatial transcriptomic
466 data. Nat Commun 13, 385.

467 Earls, R.H., Menees, K.B., Chung, J., Barber, J., Gutekunst, C.A., Hazim, M.G., and Lee, J.K. (2019).
468 Intrastriatal injection of preformed alpha-synuclein fibrils alters central and peripheral immune
469 cell profiles in non-transgenic mice. J Neuroinflammation 16, 250.

470 Frigerio, I., Bouwman, M.M.A., Noordermeer, R., Podobnik, E., Popovic, M., Timmermans, E.,
471 Rozemuller, A.J.M., van de Berg, W.D.J., and Jonkman, L.E. (2024). Regional differences in
472 synaptic degeneration are linked to alpha-synuclein burden and axonal damage in Parkinson's
473 disease and dementia with Lewy bodies. Acta Neuropathol Commun 12, 4.

474 Froula, J.M., Henderson, B.W., Gonzalez, J.C., Vaden, J.H., McLean, J.W., Wu, Y., Banumurthy, G.,
475 Overstreet-Wadiche, L., Herskowitz, J.H., and Volpicelli-Daley, L.A. (2018). alpha-Synuclein fibril-
476 induced paradoxical structural and functional defects in hippocampal neurons. Acta Neuropathol
477 Commun 6, 35.

478 Frye, H.E., Izumi, Y., Harris, A.N., Williams, S.B., Trousdale, C.R., Sun, M.Y., Sauerbeck, A.D.,
479 Kummer, T.T., Mennerick, S., Zorumski, C.F.*, et al.* (2021). Sex Differences in the Role of CNIH3
480 on Spatial Memory and Synaptic Plasticity. Biol Psychiatry 90, 766-780.

481 Gcwensa, N.Z., Russell, D.L., Long, K.Y., Brzozowski, C.F., Liu, X., Gamble, K.L., Cowell, R.M., and
482 Volpicelli-Daley, L.A. (2024). Cortico-amygdala synaptic structural abnormalities produced by
483 templated aggregation of alpha-synuclein. bioRxiv.

484 Goralski, T.M., Meyerdirk, L., Breton, L., Brasseur, L., Kurgat, K., DeWeerd, D., Turner, L., Becker,
485 K., Adams, M., Newhouse, D.J., and Henderson, M.X. (2024). Spatial transcriptomics reveals
486 molecular dysfunction associated with cortical Lewy pathology. Nature Communications 15.

487 Hänzelmann, S., Castelo, R., and Guinney, J. (2013). GSVA: gene set variation analysis for
488 microarray and RNA-seq data. BMC Bioinformatics 14, 7.

489 Hely, M.A., Reid, W.G., Adena, M.A., Halliday, G.M., and Morris, J.G. (2008). The Sydney
490 multicenter study of Parkinson's disease: the inevitability of dementia at 20 years. Mov Disord
491 23, 837-844.

492 Henderson, M.X., Cornblath, E.J., Darwich, A., Zhang, B., Brown, H., Gathagan, R.J., Sandler, R.M.,
493 Bassett, D.S., Trojanowski, J.Q., and Lee, V.M.Y. (2019). Spread of alpha-synuclein pathology
494 through the brain connectome is modulated by selective vulnerability and predicted by network
495 analysis. Nat Neurosci 22, 1248-1257.

496 Holmes, S.E., Honhar, P., Tinaz, S., Naganawa, M., Hilmer, A.T., Gallezot, J.D., Dias, M., Yang, Y.,
497 Toyonaga, T., Esterlis, I.*, et al.* (2024). Synaptic loss and its association with symptom severity in
498 Parkinson's disease. NPJ Parkinsons Dis 10, 42.

499 Iba, M., McDevitt, R.A., Kim, C., Roy, R., Sarantopoulou, D., Tommer, E., Siegars, B., Sallin, M.,
500 Kwon, S., Sen, J.M.*, et al.* (2022). Aging exacerbates the brain inflammatory micro-environment
501 contributing to alpha-synuclein pathology and functional deficits in a mouse model of DLB/PD.
502 Mol Neurodegener 17, 60.

503 Irwin, D.J., Grossman, M., Weintraub, D., Hurtig, H.I., Duda, J.E., Xie, S.X., Lee, E.B., Van Deerlin,
504 V.M., Lopez, O.L., Kofler, J.K*., et al.* (2017). Neuropathological and genetic correlates of survival
505 and dementia onset in synucleinopathies: a retrospective analysis. Lancet Neurol 16, 55-65.

506 Irwin, D.J., White, M.T., Toledo, J.B., Xie, S.X., Robinson, J.L., Van Deerlin, V., Lee, V.M., Leverenz,
507 J.B., Montine, T.J., Duda, J.E*., et al.* (2012). Neuropathologic substrates of Parkinson disease
508 dementia. Ann Neurol 72, 587-598.

509 Koopmans, F., van Nierop, P., Andres-Alonso, M., Byrnes, A., Cijsouw, T., Coba, M.P., Cornelisse,
510 L.N., Farrell, R.J., Goldschmidt, H.L., Howrigan, D.P*., et al.* (2019). SynGO: an evidence-based,
511 expert-curated knowledge base for the synapse. Neuron 103, 217-234 e214.

512 Kramer, M.L., and Schulz-Schaeffer, W.J. (2007). Presynaptic alpha-synuclein aggregates, not
513 Lewy bodies, cause neurodegeneration in dementia with Lewy bodies. J Neurosci 27, 1405-1410.

514 Li, J., Zhang, Y., Huang, Z., Jiang, Y., Ren, Z., Liu, D., Zhang, J., La Piana, R., and Chen, Y. (2022).
515 Cortical and subcortical morphological alterations in motor subtypes of Parkinson's disease. NPJ
516 Parkinsons Dis 8, 167.

517 Lu, J., Wang, C., Cheng, X., Wang, R., Yan, X., He, P., Chen, H., and Yu, Z. (2022). A breakdown in
518 microglial metabolic reprogramming causes internalization dysfunction of alpha-synuclein in a
519 mouse model of Parkinson's disease. J Neuroinflammation 19, 113.

520 Luk, K.C., Kehm, V., Carroll, J., Zhang, B., O'Brien, P., Trojanowski, J.Q., and Lee, V.M. (2012).
521 Pathological alpha-synuclein transmission initiates Parkinson-like neurodegeneration in
522 nontransgenic mice. Science 338, 949-953.

523 Matuskey, D., Tinaz, S., Wilcox, K.C., Naganawa, M., Toyonaga, T., Dias, M., Henry, S., Pittman, B.,
524 Ropchan, J., Nabulsi, N*., et al.* (2020). Synaptic Changes in Parkinson Disease Assessed with in
525 vivo Imaging. Ann Neurol 87, 329-338.

526 Pérez-Acuña, D., Shin, S.J., Rhee, K.H., Kim, S.J., and Lee, S.J. (2023). alpha-Synuclein propagation
527 leads to synaptic abnormalities in the cortex through microglial synapse phagocytosis. Mol Brain
528 16, 72.

529 Poewe, W., Seppi, K., Tanner, C.M., Halliday, G.M., Brundin, P., Volkmann, J., Schrag, A.E., and
530 Lang, A.E. (2017). Parkinson disease. Nat Rev Dis Primers 3, 17013.

531 Recasens, A., Dehay, B., Bove, J., Carballo-Carbajal, I., Dovero, S., Perez-Villalba, A., Fernagut,
532 P.O., Blesa, J., Parent, A., Perier, C*., et al.* (2014). Lewy body extracts from Parkinson disease
533 brains trigger alpha-synuclein pathology and neurodegeneration in mice and monkeys. Ann
534 Neurol 75, 351-362.

535 Reitz, S.J., Sauerbeck, A.D., and Kummer, T.T. (2021). SEQUIN: An imaging and analysis platform
536 for quantification and characterization of synaptic structures in mouse. STAR Protoc 2, 100268.

537 Ryman, S.G., Yutsis, M., Tian, L., Henderson, V.W., Montine, T.J., Salmon, D.P., Galasko, D., and
538 Poston, K.L. (2021). Cognition at Each Stage of Lewy Body Disease with Co-occurring Alzheimer's
539 Disease Pathology. J Alzheimers Dis 80, 1243-1256.

Sauerbeck, A.D., Gangolli, M., Reitz, S.J., Salyards, M.H., Kim, S.H., Hemingway, C., Gratuze, M., Makkapati, T., Kerschensteiner, M., Holtzman, D.M*., et al.* (2020). SEQUIN multiscale imaging of mammalian central synapses reveals loss of synaptic connectivity resulting from diffuse traumatic brain injury. Neuron 107, 257-273 e255.

Schapira, A.H.V., Chaudhuri, K.R., and Jenner, P. (2017). Non-motor features of Parkinson disease. Nat Rev Neurosci 18, 435-450.

Schirinzi, T., Madeo, G., Martella, G., Maltese, M., Picconi, B., Calabresi, P., and Pisani, A. (2016). Early synaptic dysfunction in Parkinson's disease: Insights from animal models. Mov Disord 31, 802-813.

Stoyka, L.E., Arrant, A.E., Thrasher, D.R., Russell, D.L., Freire, J., Mahoney, C.L., Narayanan, A., Dib, A.G., Standaert, D.G., and Volpicelli-Daley, L.A. (2020). Behavioral defects associated with amygdala and cortical dysfunction in mice with seeded alpha-synuclein inclusions. Neurobiol Dis 134, 104708.

Thomsen, M.B., Jacobsen, J., Lillethorup, T.P., Schacht, A.C., Simonsen, M., Romero-Ramos, M., Brooks, D.J., and Landau, A.M. (2021). In vivo imaging of synaptic SV2A protein density in healthy and striatal-lesioned rats with [11C]UCB-J PET. J Cereb Blood Flow Metab 41, 819-830.

Vargas, K.J., Schrod, N., Davis, T., Fernandez-Busnadiego, R., Taguchi, Y.V., Laugks, U., Lucic, V., and Chandra, S.S. (2017). Synucleins Have Multiple Effects on Presynaptic Architecture. Cell Rep 18, 161-173.

Volpicelli-Daley, L.A., Luk, K.C., and Lee, V.M. (2014). Addition of exogenous alpha-synuclein preformed fibrils to primary neuronal cultures to seed recruitment of endogenous alpha-synuclein to Lewy body and Lewy neurite-like aggregates. Nat Protoc 9, 2135-2146.

Volpicelli-Daley, L.A., Luk, K.C., Patel, T.P., Tanik, S.A., Riddle, D.M., Stieber, A., Meaney, D.F., Trojanowski, J.Q., and Lee, V.M. (2011). Exogenous alpha-synuclein fibrils induce Lewy body pathology leading to synaptic dysfunction and neuron death. Neuron 72, 57-71.

Wu, Q., Takano, H., Riddle, D.M., Trojanowski, J.Q., Coulter, D.A., and Lee, V.M. (2019). alpha-Synuclein (alphaSyn) Preformed Fibrils Induce Endogenous alphaSyn Aggregation, Compromise Synaptic Activity and Enhance Synapse Loss in Cultured Excitatory Hippocampal Neurons. J Neurosci 39, 5080-5094.

Zhan, S.S., Beyreuther, K., and Schmitt, H.P. (1993). Quantitative assessment of the synaptophysin immuno-reactivity of the cortical neuropil in various neurodegenerative disorders with dementia. Dementia 4, 66-74.

Figure Legends

Figure 1. Progressive loss of cortical excitatory synapses in the PFF mouse model stratingat 3 months post-PFF injection.

(A) Model of striatal PFF injection to assess the impact of cortical pathology.

(B-D) Left, 3D reconstructed images of excitatory presynaptic VGluT1 (green) and excitatory postsynaptic Homer (red) in the cortex after (B) 1 month, (C) 3 months, and (D) 6 months of monomer vs. PFF injection. Right, differences in paired synaptic loci density are denoted by the p-value (Mann-Whitney test) for PFF vs. monomer injection. VGluT1 and Homer-positive puncta densities were analyzed based on puncta intensities and are shown as mean ± SEM. B,C, n = 3 animals/group, 6-8 slices per animal. D, n = 6 animals/group, 6-8 slices per animal.

Figure 2. Reduction of excitatory synaptic specializations.

Images as in Figure 1 were analyzed for the density of individual excitatory pre- and post-synaptic specializations, including those scored as paired and isolated. No reduction was observed after 1 MPI (A), but excitatory pre- and post-synaptic specializations were less abundant at 3 MPI (B). No change was detected at 6 MPI.

Figure 3. Inhibitory postsynaptic Gephyrin is reduced in the cortex at 6 months post-injection.

(A, B) vGAT- and gephyrin-positive puncta densities were analyzed based on puncta intensities after (A) 3 months and (B) 6 months post-injection. Densities for vGAT, gephyrin, and synaptic loci are shown as mean ± SEM. (A) n = 3 animals/group, 7-9 slices per animal). (B) n = 4 animals/group, 7-9 slices per animal.

Figure 4. Phospho-α-synuclein accumulates at synaptic loci and is associated with synapse loss.

(A) Representative images of 3D imaging fields for PSD-95, synapsin, and phospho-α-synuclein.

(B) High magnification 2D projection 600nm thick showing overlap of pre- and post-synaptic proteins with phospho-α-synuclein.

(C) Schematic of methodology for measuring phospho-α-synuclein in 200 nm fields centered on synaptic loci.

(D) Quantification of synapse-associated and parenchymal phospho-α-synuclein from synuclein monomer and synuclein PFF treated animals across all tiles and regions of low and high relative pathology. Dark symbols are individual image tiles and red symbols are medians for each animal.

(E) Ratio of synaptic associated versus parenchymal phospho-α-synuclein staining in areas with low, mid, and high total phospho-α-synuclein pathology. Dark symbols are individual image tiles and red symbols are the median for each animal.

(F-H) Representative image of area of tilescan performed 1-month post monomer or PFF injection (PFF-injected animal depicted). Maximum intensity projection of mesoscan from monomer (G) and PFF (H) injected animals. Images correspond to boxed area in (F).

(I-J) Heatmaps of synapse-associated phospho-α-synuclein and synaptic density 1-month after injection of synuclein PFFs.

(K-L) Heatmaps of synapse-associated phospho-α-synuclein and synaptic density 1-month after injection of synuclein monomers. Boxed region in (J) used for analysis in (M-Q). Group-wise analysis of synaptic density (M) and parenchymal phospho-α-synuclein (N) between monomer and PFF injected animals. Statistics performed on red symbols representative of group averages and not individual tiles.
(O-Q) Within animal correlations of synaptic density with synapse-associated phospho-α-synuclein (subjects 1-3 left to right). Spearman's ρ -0.50, -0.65, 0.81 subject 1, 2, and 3, respectively. Scale bars: (A):5 µm, (B):425 nm, (F): 1000 µm, (G,H): 250 µm, (I-L): 250 µm.

Figure 5. Lewy neurite pathology influences the density and phospho-α-synuclein content of local synapses.
(A) Representative image of pSD-95, synapsin, and phospho-α-synuclein 1 month following synuclein PFF injection.
(B) Masking of Lewy neurites for measurement of distance between synaptic loci and neurite borders.
(C) Schematic corresponding to boxed region in (B) showing distance measurement from synaptic centroids and borders of Lewy neurite masks.
(D) Quantification of synaptic phospho-α-synuclein enrichment as a function of distance to a Lewy neurite.
(E) The extent of pathology in Lewy neurites (phospho-α-synuclein intensity) is anticorrelated with the density of synaptic loci in its vicinity (within 800 nm of a neurite edge) (Spearman's ρ -0.92).

Figure 6. Dysregulation of synaptic pathways in phospho-α-synuclein bearing neurons.
(A) Volcano plot of SynGO annotated genes differentially expressed in phospho-α-synuclein immunopositive neurons.
(B, D) Enrichment of synaptic pathways in phospho-α-synuclein pathology bearing neurons. Sunburst plots illustrate cellular components and biological processes from downregulated and upregulated DEGs.
(C) Bar plots illustrates top enriched GO terms within categories: Synaptic Organization, Process in the presynapse and Process in the postsynapse

Figure 7. Apparent increase in pre-post synaptic separation with ultrastructural changes in the excitatory synapse as pathology progresses.
(A) Apparent increase in pre-post synaptic separation for VGluT1/Homer-positive synaptic loci was analyzed by determining the mean distance from Gaussian distribution of synaptic loci after PFF vs. monomer injection at 3 months post-injection (n = 3 animals/group, 6-8 slices per animal, *p, Mann-Whitney test compared to monomer-injected mice).
(B) Ultrastructural analysis of synaptic vesicle size in PFF-injected mice compared to control mice injected with PBS using transmission electron microscopy.

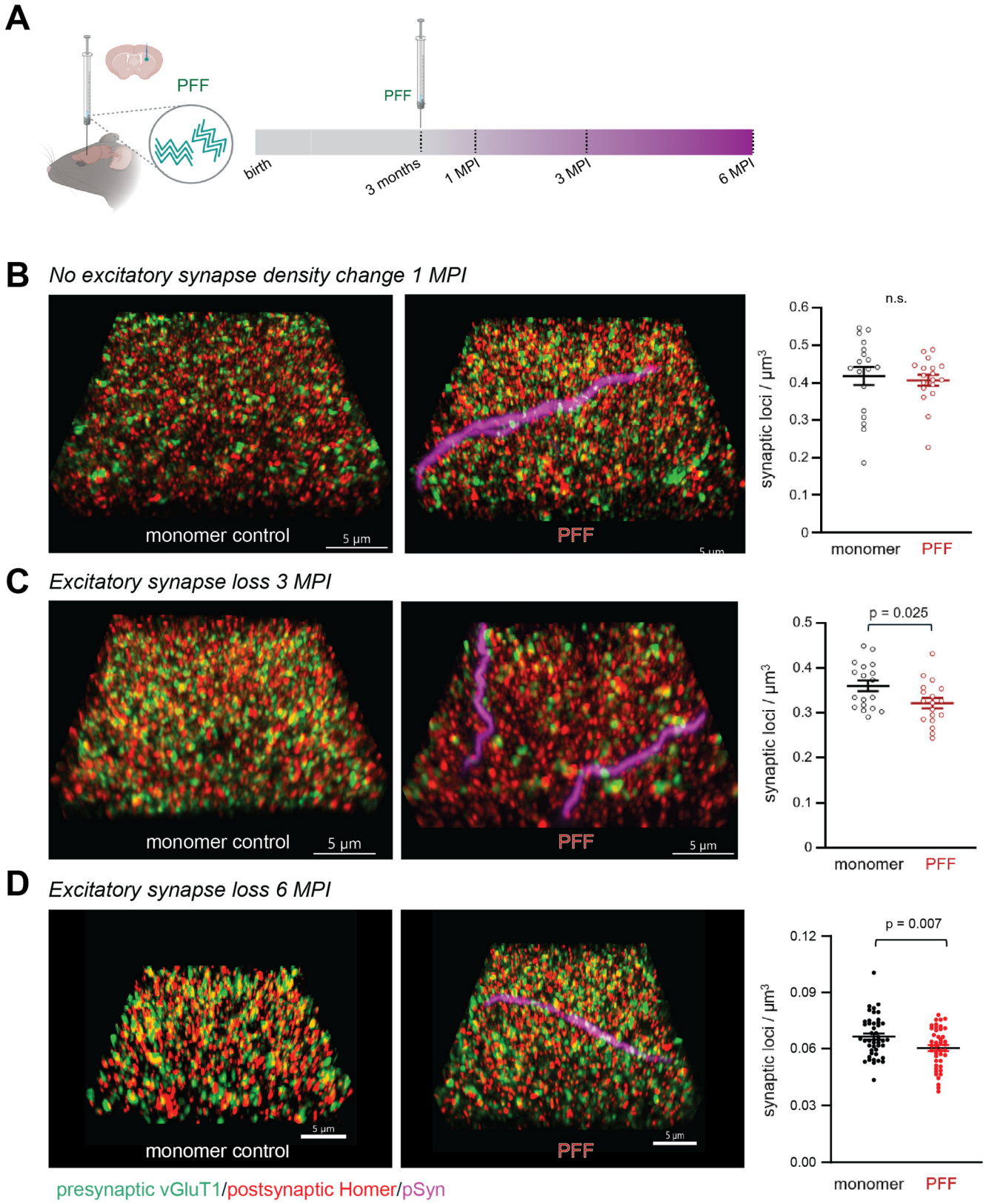
A
PFF
PFF
birth
3 months
1 MPI
3 MPI
6 MPI
B
No excitatory synapse density change 1 MPI
monomer control
5 µm
PFF
n.s.
synaptic loci / µm³
0.6
0.5
0.4
0.3
0.2
0.1
0
monomer
PFF
C
Excitatory synapse loss 3 MPI
monomer control
5 µm
PFF
5 µm
p = 0.025
synaptic loci / µm³
0.5
0.4
0.3
0.2
0.1
0
monomer
PFF
D
Excitatory synapse loss 6 MPI
5 µm
monomer control
5 µm
PFF
p = 0.007
synaptic loci / µm³
0.12
0.09
0.06
0.03
0.00
monomer
PFF
presynaptic vGluT1/postsynaptic Homer/pSyn

Figure 1

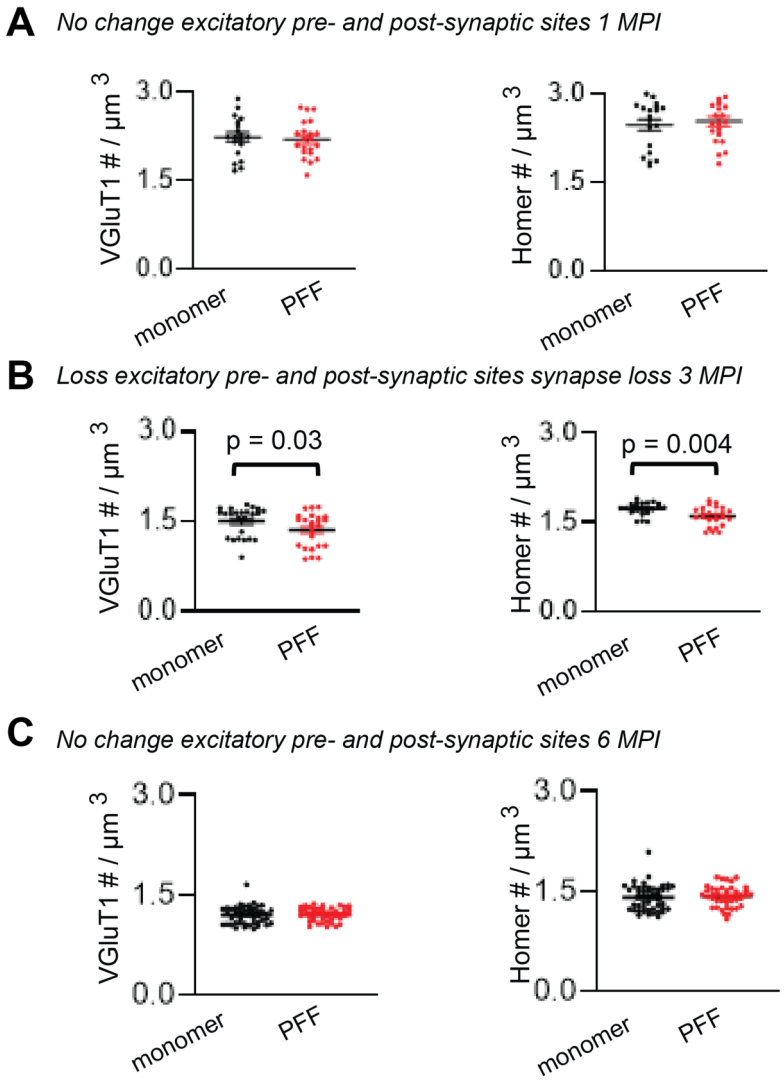
A
No change excitatory pre- and post-synaptic sites 1 MPI
VGluT1 # / µm 3
3.0
1.5
0.0
monomer
PFF
Homer # / µm 3
3.0
1.5
0.0
monomer
PFF
B
Loss excitatory pre- and post-synaptic sites synapse loss 3 MPI
VGluT1 # / µm 3
3.0
1.5
0.0
p = 0.03
monomer
PFF
Homer # / µm 3
3.0
1.5
0.0
p = 0.004
monomer
PFF
C
No change excitatory pre- and post-synaptic sites 6 MPI
VGluT1 # / µm 3
3.0
1.5
0.0
monomer
PFF
Homer # / µm 3
3.0
1.5
0.0
monomer
PFF

Figure 2

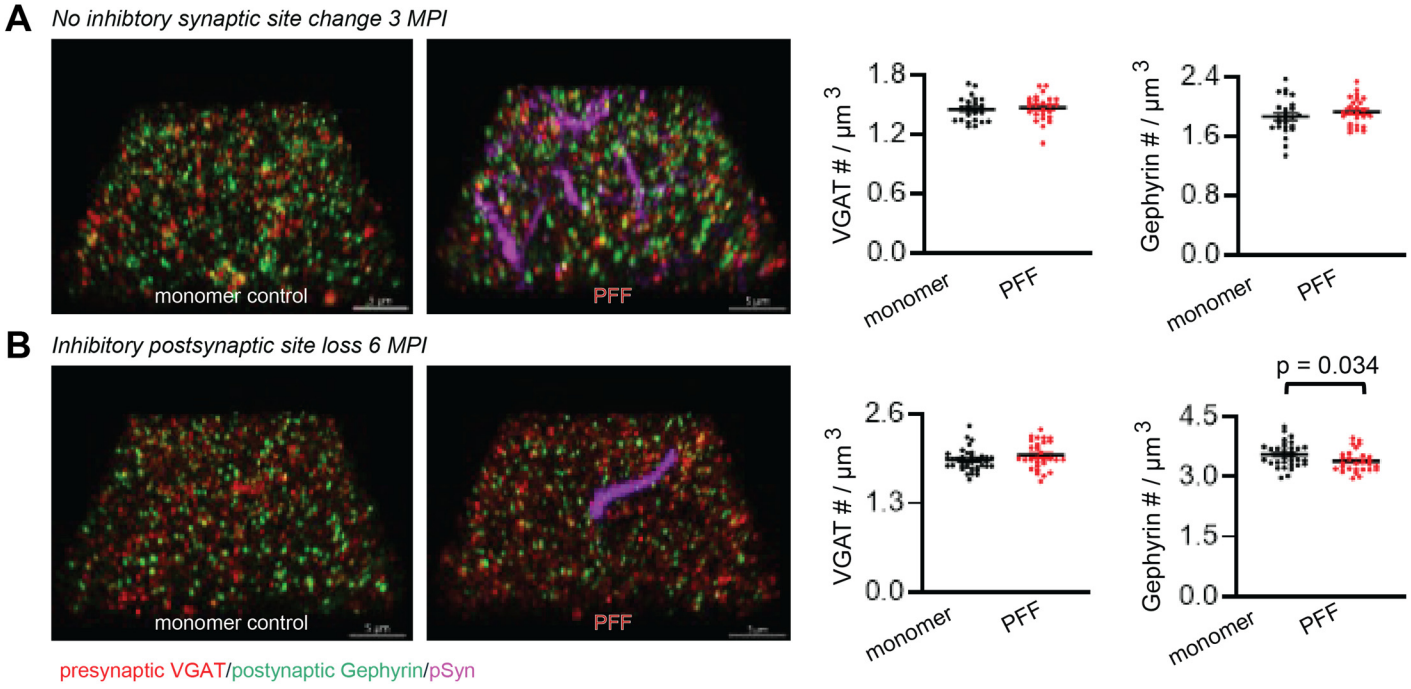
A
No inhibtory synaptic site change 3 MPI
monomer control
PFF
B
Inhibitory postsynaptic site loss 6 MPI
monomer control
PFF
presynaptic VGAT/postynaptic Gephyrin/pSyn
VGAT # / µm 3
1.8
1.2
0.6
0.0
monomer
PFF
Gephyrin # / µm 3
2.4
1.6
0.8
0.0
monomer
PFF
VGAT # / µm 3
2.6
1.3
0.0
monomer
PFF
p = 0.034
Gephyrin # / µm 3
4.5
3.0
1.5
0.0
monomer
PFF

Figure 3

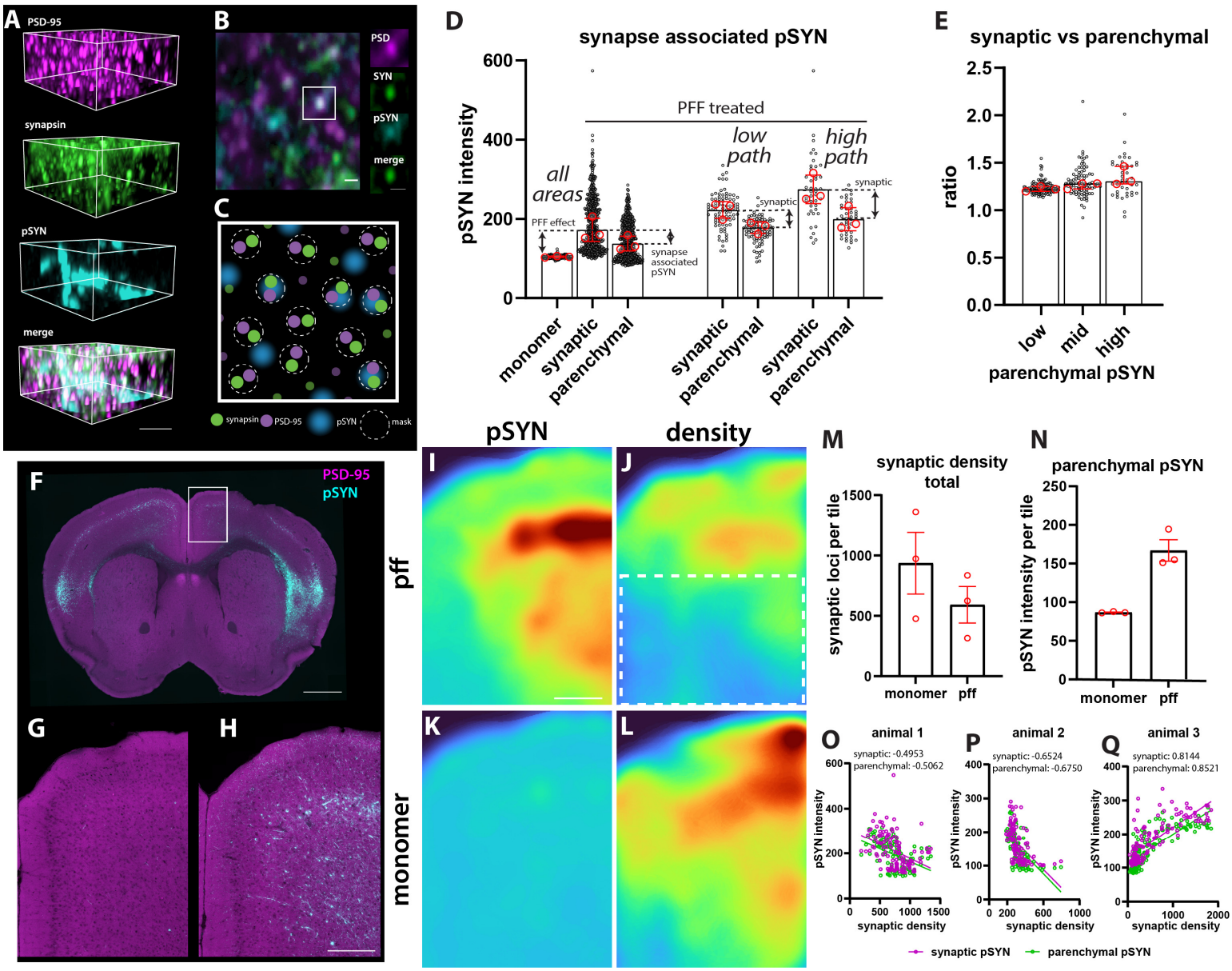
A
PSD-95
synapsin
pSYN
merge
B
PSD
SYN
pSYN
merge
C
synapsin
PSD-95
pSYN
mask
D
synapse associated pSYN
pSYN intensity
PFF treated
all areas
low path
high path
PFF effect
synaptic
synapse associated pSYN
monomer
synaptic
parenchymal
E
synaptic vs parenchymal
ratio
low
mid
high
parenchymal pSYN
F
PSD-95
pSYN
G
H
pSYN
density
pff
monomer
I
J
K
L
M
synaptic density total
synaptic loci per tile
monomer
pff
N
parenchymal pSYN
pSYN intensity per tile
O
animal 1
synaptic: -0.4953
parenchymal: -0.5062
P
animal 2
synaptic: -0.6524
parenchymal: -0.6750
Q
animal 3
synaptic: 0.8144
parenchymal: 0.8521
synaptic density
synaptic pSYN
parenchymal pSYN

Figure 4

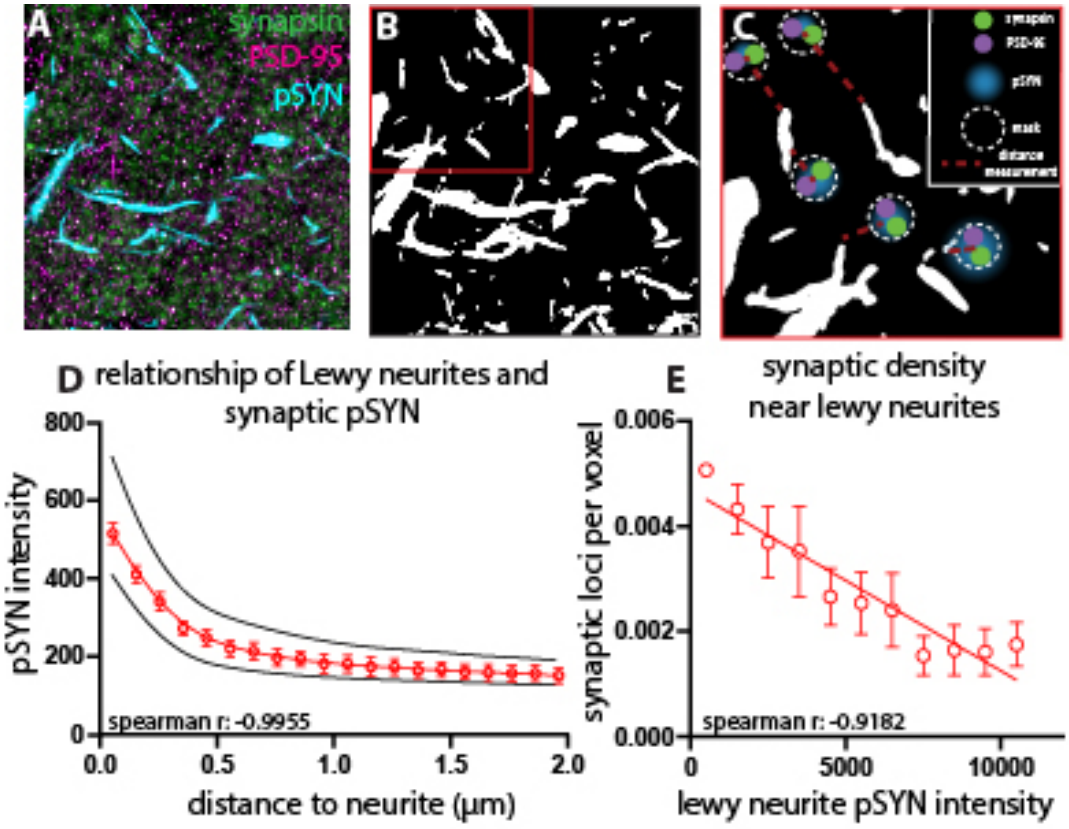

666

667 **Figure 5**

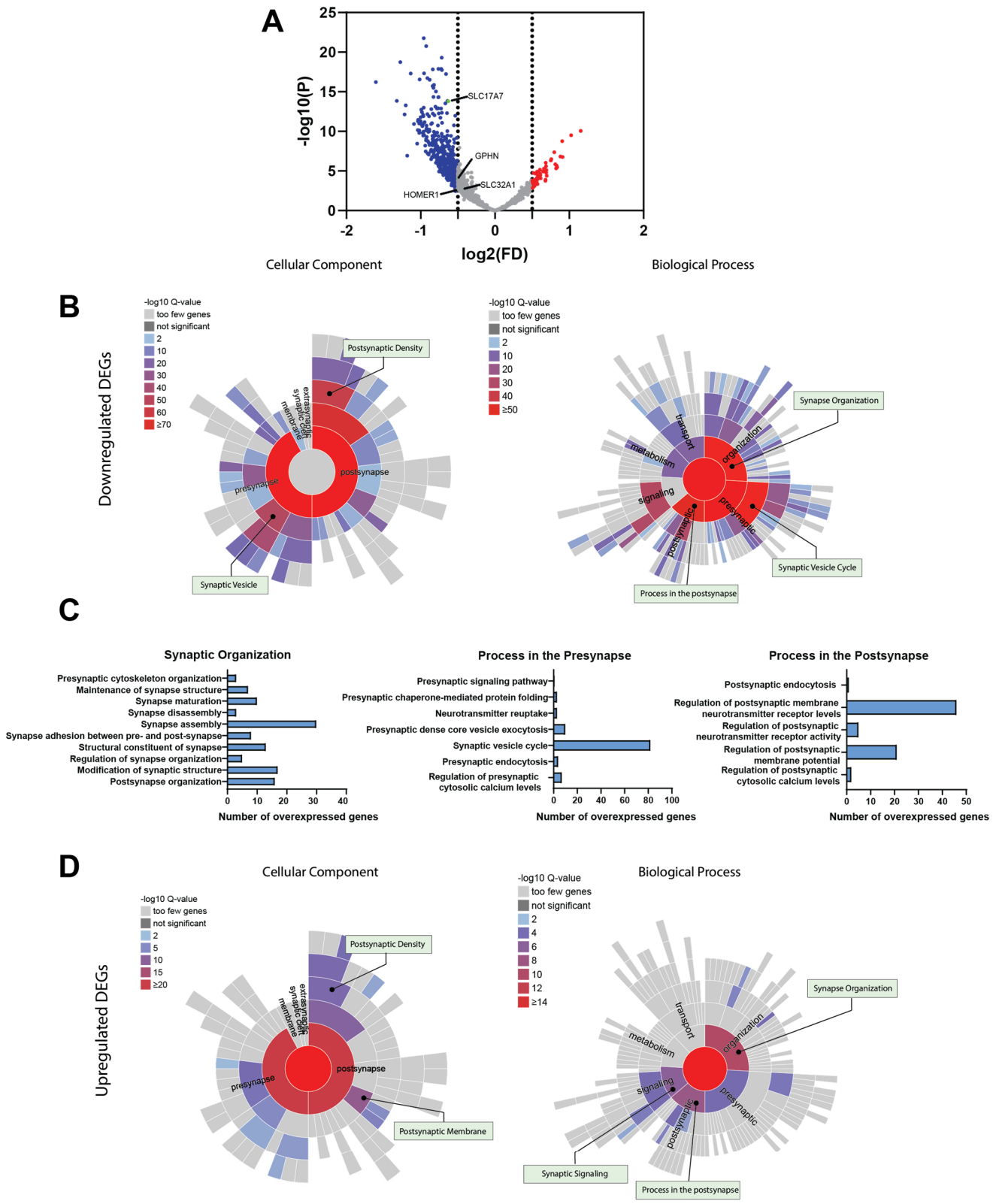
A
-log10(P)
log2(FD)
SLC17A7
GPHN
SLC32A1
HOMER1
Cellular Component
Biological Process
B
Downregulated DEGs
-log10 Q-value
too few genes
not significant
Postsynaptic Density
extracellular
synaptic cleft
membrane
presynapse
postsynapse
Synaptic Vesicle
Synapse Organization
transport
metabolism
organization
signaling
presynaptic
postsynaptic
Synaptic Vesicle Cycle
Process in the postsynapse
C
Synaptic Organization
Presynaptic cytoskeleton organization
Maintenance of synapse structure
Synapse maturation
Synapse disassembly
Synapse assembly
Synapse adhesion between pre- and post-synapse
Structural constituent of synapse
Regulation of synapse organization
Modification of synaptic structure
Postsynapse organization
Number of overexpressed genes
Process in the Presynapse
Presynaptic signaling pathway
Presynaptic chaperone-mediated protein folding
Neurotransmitter reuptake
Presynaptic dense core vesicle exocytosis
Synaptic vesicle cycle
Presynaptic endocytosis
Regulation of presynaptic cytosolic calcium levels
Number of overexpressed genes
Process in the Postsynapse
Postsynaptic endocytosis
Regulation of postsynaptic membrane neurotransmitter receptor levels
Regulation of postsynaptic neurotransmitter receptor activity
Regulation of postsynaptic membrane potential
Regulation of postsynaptic cytosolic calcium levels
Number of overexpressed genes
D
Upregulated DEGs
Cellular Component
-log10 Q-value
too few genes
not significant
Postsynaptic Density
extracellular
synaptic cleft
membrane
presynapse
postsynapse
Postsynaptic Membrane
Biological Process
Synapse Organization
transport
metabolism
organization
signaling
presynaptic
postsynaptic
Synaptic Signaling
Process in the postsynapse

Figure 6

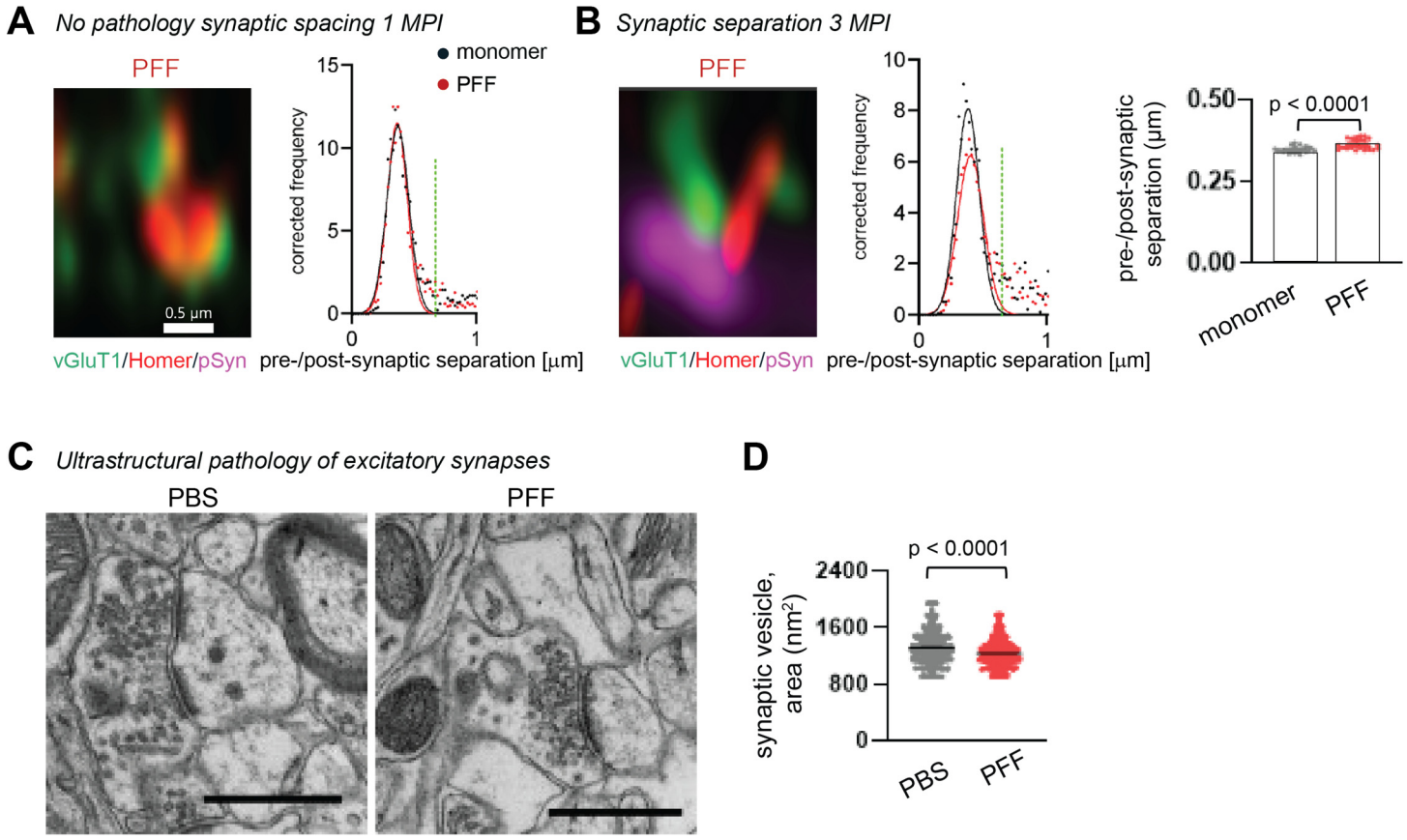

670

671 **Figure 7**